Acta Mech 229, 3355–3373 (2018)
https://doi.org/10.1007/s00707-018-2165-8

ORIGINAL PAPER

P. A. Roy · S. A. Meguid

Analytical modeling of the coupled nonlinear free vibration response of a rotating blade in a gas turbine engine

Received: 21 November 2017 / Revised: 13 February 2018 / Published online: 17 May 2018

Abstract In this paper, we investigate the free vibration response of a rotating blade in a gas turbine engine. The blade is modeled as a tapered Timoshenko beam with nonlinear variations in its cross-section properties. The governing equations of motions are derived using Lagrangian mechanics and Rayleigh–Ritz method. These equations take into account centrifugal stiffening, axial and lateral coupling due to Coriolis effect, shear deformation, and rotary inertia. We examine the effect of the beam geometry upon its axial and lateral free vibration response. The effects of rotational speed, taper ratio, chord ratio, hub radius, and slenderness ratio on the natural frequencies are analyzed. The results of our analysis indicate that the taper ratio, slenderness ratio, and rotational speed of the beam govern its free lateral vibration response. The axial vibration of the beam is significantly affected by the slenderness ratio, but it is found to be independent of the hub radius.

List of symbols

A	Cross-section area of the beam
A_a	Coefficients for polynomial of the cross-section area
A_r	Cross-section area of the beam at the hub
$\mathbf{C}$	Coriolis damping matrix
E	Young's modulus
F_{cf}	Centrifugal force
G	Shear modulus
I	Area moment of inertia
I_a	Coefficients for polynomial of the moment of inertia
I_r	Moment of inertia of the beam at the hub
$\mathbf{K}$	Total stiffness matrix
$\mathbf{K^m}$	Elastic property-dependent stiffness matrix
$\mathbf{K^\Omega}$	Rotational speed-dependent stiffness matrix
L	Length of the beam
$\mathbf{M}$	Mass matrix
P	Force vector
R	Radius of the tip of the beam
T	Kinetic energy of the beam
$\mathbf{T}$	Transformation matrix
U	Total potential energy

P. A. Roy · S. A. Meguid (✉)
Mechanics and Aerospace Design Laboratory, Department of Mechanical and Industrial Engineering, University of Toronto, 5 King's College Rd, Toronto, ON M5S 3G8, Canada
E-mail: meguid@mie.utoronto.ca

U_W	Work done by applied forces
U_γ	Potential energy due to shear strain
U_ε	Potential energy due to axial strain
W, U, Φ	Displacement component of shape functions
X, Y, Z	Time-dependent generalized coordinates
c	Chord length
c_R	Chord length at the tip
c_r	Chord length at the hub
$\bar{c}$	Chord ratio
$(\hat{e}_z, \hat{e}_s, \hat{e}_c)$	Rotating coordinate system
$\mathbf{d}$	Displacement field vector
h	Thickness of the beam
h_R	Thickness of the beam at the tip
h_r	Thickness of the beam at the hub
$\bar{h}$	Taper ratio
k	Shear coefficient
m	Mass of the beam
n_A	Index of order of polynomial for area
n_I	Index of order of polynomial for moment of inertia
r	Radius of the hub of the beam
$\mathbf{r}$	Position vector of a typical point on the beam in stationary coordinate system
$\mathbf{r_r}$	Position vector of a typical point on the beam in rotating coordinate system
$\bar{r}$	Non-dimensional hub radius
s	Span of the beam
u	Axial displacement
$\mathbf{v}$	Velocity vector
w	Lateral displacement
z	Distance of a typical fiber of the beam on a given cross-section area along lateral direction
Λ	Lagrangian
Ω	Rotational speed
$\bar{\Omega}$	Non-dimensional rotational speed
β	Stagger angle of the beam
γ_{sz}	Shear strain
$\boldsymbol{\varepsilon}$	Linear strain tensor
ε_s	Axial strain
θ	Rotational angle Ωt
$\{\xi\}$	Generalized coordinate
ρ	Density
φ	cross-section rotation
ω_n	Natural frequency (rad/s)
$\bar{\omega}_n$	Non-dimensional natural frequency

1 Introduction

Rotating blades are employed in several engineering applications of turbomachinery such as compressors and turbines disk assemblies. The free vibration analysis of these blades is crucial to determine their dynamic response and stability in operation. Traditionally, the natural frequencies of these blades are analyzed by modeling blades as rotating cantilever beams. However, the presence of centrifugal stiffening, coupling of axial and lateral displacements and non-uniform cross-section properties of the beams present challenges to the derivation of an accurate analytical formulation. Therefore, a number of authors have attempted to analyze the problem, with numerous simplifications in the geometry of the beam or in the definition of the problem, or both. Both Euler–Bernoulli beam and Timoshenko beam have been used to model the problem. Timoshenko beam theory takes into account rotary inertia and shear deformation and provides more accurate results than Euler–Bernoulli beam theory. However, the available papers over-simplify the cross section of the beam and ignore the axial vibration mode. A brief summary of the literature is presented below to support our case.

We will divide these articles into two main categories: Euler–Bernoulli beams where shear effects are ignored and Timoshenko beams where the authors accounted for shear effects and rotary inertia. Examples of the articles employing Euler–Bernoulli include the work of Hodges et al. [1], Wang et al. [2], Bazoune [3], Zhou et al. [4], Ece et al. [5], and Mao et al. [6] who conducted the free vibration analysis of non-rotating beams with linear and nonlinear cross-section variations. Kane et al. [7], Khulief [8], Naguleswaran [9], Yang et al. [10], Banerjee et al. [11,12], Wang et al. [13], Ozgumus et al. [14], Attarnejad et al. [15], Firouz-abadi et al. [16] and Lee et al. [17] analyzed the lateral vibration response of rotating beams with linear taper in height and width under different boundary conditions. Vinod et al. [18] used the approximate spectral element method for the free vibration analysis of beams of mass and stiffness variations. Fung et al. [19] studied the effect of centrifugal force on the frequencies of a rotating arm with an end mass and axial force. Huang et al. [20] used a power series solution to describe the lateral vibration of tapered beams with coupled axial and lateral deformations. Liao et al. [21] performed the stability analysis of a pre-twisted beam rotating about its longitudinal axis with axial forces of periodic fluctuations. Sarkar et al. [22] derived a closed form solution for the free vibration of non-uniform beams for special cases of free–free boundary conditions.

A number of authors have modeled the blade as a Timoshenko beam [23], which unlike an Euler–Bernoulli beam accounts for the effects of shear deformation and rotary inertia. Some of the important studies of Timoshenko beams include the works of Lee et al. [24], Auciello et al. [25], Yuan et al. [26], Ozgumus et al. [27], Zhou et al. [28], and Huang et al. [29] who performed the free vibration analysis of stationary tapered beams. Abbas [30], Datta et al. [31], Ozgumus et al. [32,33], Zhu et al. [34], Lee et al. [35], Rajsekaran et al. [36], and Chen et al. [37] presented the free lateral vibration analysis of rotating beams with linear taper in both height and width. Lee et al. [38], Chen et al. [39] and Yardimoglu et al. [40] presented results on the dynamic stability of a rotating pre-twisted beam under a constant axial force. Lin et al. [41] and Lee et al. [42] analyzed the effect of Coriolis forces on the free vibration response of a rotating uniform beam. Ibrahim et al. [43] used a unified beam theory for Euler–Bernoulli and Timoshenko beams to derive the free lateral vibration response of square and circular tapered beams. Ghafarian et al. [44] derived a solution for elastically connected rotating tapered beams. Yardimoglu et al. [45] used the finite element theory with coupled displacement field for nonlinear tapered beams.

Our careful review of the literature indicates that the majority of the existing works deal with only linearly tapered beams and considers the lateral vibration response of the blade. There are only a few articles which include the effect of Coriolis coupling effects for uniform beams. To the best of the authors' knowledge, no research work currently exists that examines the free vibration response of a non-uniform Timoshenko beam with nonlinear thickness variation and coupling of the axial and the lateral displacements that takes into account rotary inertia and shear deformation. The present paper aims to fill that gap.

2 Governing equations of motion

The analytical formulation is derived for a blade assumed as a rotating Timoshenko beam fixed at the hub. The beam is assumed to be of rectangular cross-section geometry with reduced thickness and/or chord (width) from the hub to the tip, as shown in Fig. 1; noting that r is the inner radius of the beam, R is the outer radius of the beam, and Ω is its rotational speed. The nonlinear variations in the cross-section area and second moment of inertia are expressed as polynomial functions of span s of the beam, as presented by Eqs. (1) and (2),

$$A(s) = \sum_{a=0}^{n_A} A_a s^a, \tag{1}$$

$$I(s) = \sum_{a=0}^{n_I} I_a s^a. \tag{2}$$

These polynomials would allow the generalized modeling of the beam.

The centrifugal force at a general span s of the beam can be expressed as

$$F_{\mathrm{cf}}(s) = \rho\Omega^2 \sum_{a=0}^{n_A} \frac{A_a}{(a+1)(a+2)} \left[L^{(a+1)} \{(a+1) R + r\} - s^{(a+1)} \{(a+2) r + (a+1) s\} \right]. \tag{3}$$

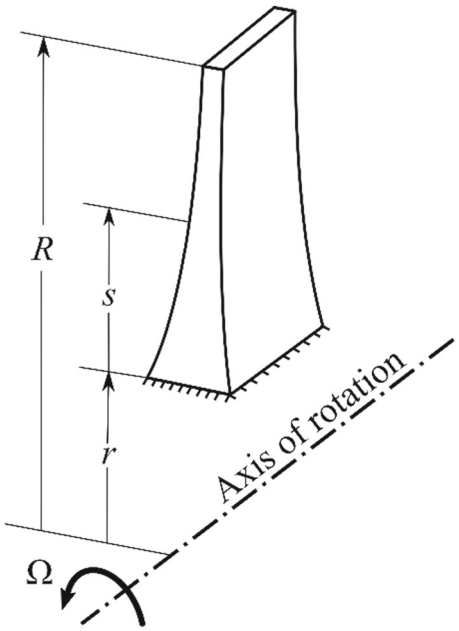

Fig. 1 A schematic of the rotating non-uniform cantilever beam considered in the study

The first derivative of the centrifugal force with respect to span s is given by

$$\frac{\partial F_{\mathrm{cf}}(s)}{\partial s} = -\rho\Omega^2 \sum_{a=0}^{n_A} A_a (r+s)\, s^a \tag{4}$$

where L is the length of the beam with $L = R - r$.

Figure 2 shows a non-uniform Timoshenko beam with a stagger angle β clamped at the hub. Two coordinate systems are defined to facilitate the analytical formulation: (i) a stationary coordinate system $(\hat{i}, \hat{j}, \hat{k})$ with an origin at the center of the rotor, as shown in Fig. 2a, and (ii) a rotating coordinate system $(\hat{e}_z, \hat{e}_s, \hat{e}_c)$ with the origin at the clamped end of the beam, as shown in Fig. 2b. The deformation at any point along the span of the beam is defined in terms of the lateral displacement w, axial displacement u, and cross-section rotation φ in a rotating coordinate system. These displacements are assumed to be functions of the span of the beam s and the time t. The deformation in the chord direction (i.e., $\hat{e}_c$-coordinate in Fig. 2b) is assumed to be zero in this analysis. The schematic diagram of a clamped Timoshenko beam in a centrifugal force field is shown in Fig. 3 with an axial displacement u, lateral displacement w, and cross-section rotation φ.

The displacement field $\mathbf{d}$ of a typical point on the beam at span s and distance z from the midplane in the rotating coordinate system $(\hat{e}_z, \hat{e}_s, \hat{e}_c)$ is defined as

$$\mathbf{d} = \{w, u - z\varphi, 0\}^T . \tag{5}$$

From Eq. (5), we can obtain the strain tensor $\boldsymbol{\varepsilon}$ as

$$\boldsymbol{\varepsilon} = \frac{1}{2}\left(\nabla\mathbf{d} + \nabla^T\mathbf{d}\right) = \begin{bmatrix} 0 & \frac{1}{2}(w' - \varphi) & 0 \\ \frac{1}{2}(w' - \varphi) & (u' - z\varphi') & 0 \\ 0 & 0 & 0 \end{bmatrix}. \tag{6}$$

The strain tensor given by (6) shows that the axial strain ε_{s} and the shear strain γ_{sz} are:

$$\varepsilon_{\mathrm{s}} = (u' - z\varphi'), \tag{7}$$

$$\gamma_{sz} = (w' - \varphi). \tag{8}$$

Lagrangian principle is used to derive the governing equations of motion such that the Lagrangian $\Lambda = T - U$. T and U are the kinetic energy and potential energy of the system, respectively. For the present case,

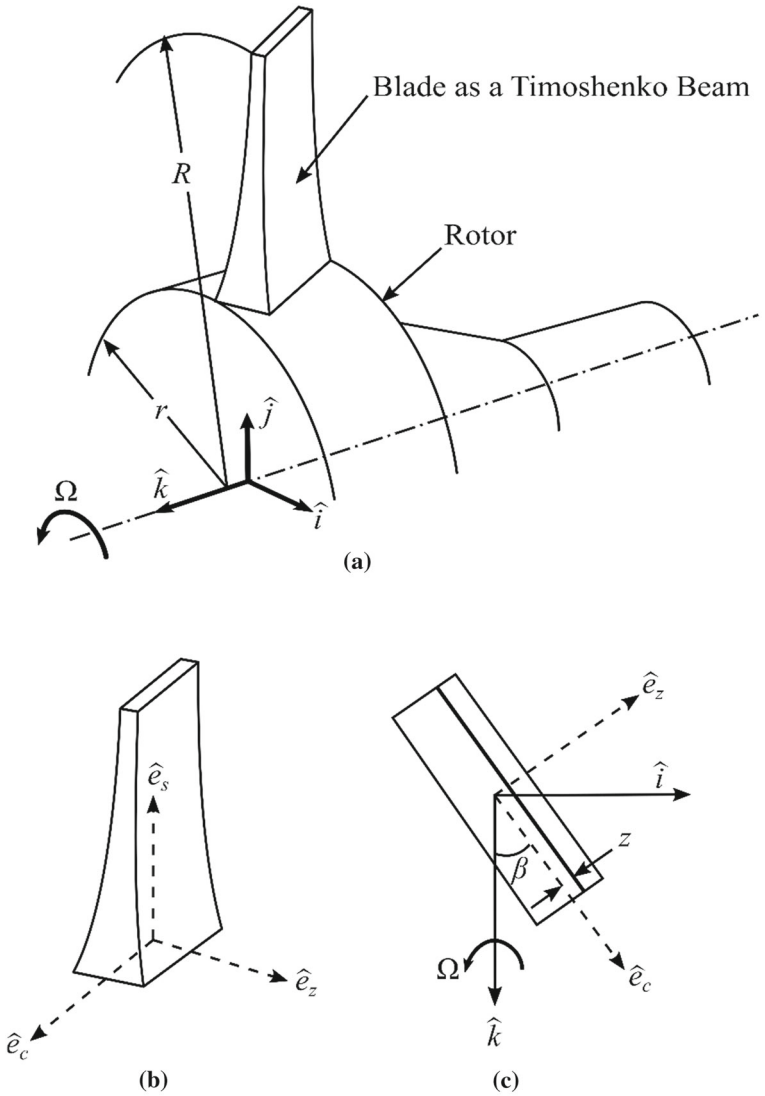

Fig. 2 A schematic view of a blade modeled as a Timoshenko beam: **a** a blade fixed to a rotor as a beam, **b** a rotating coordinate system, and **c** a typical cross section of a beam

the Lagrangian Λ is of the form $\Lambda = \Lambda\left(t, s, x_i, \dot{x}_i, x_i'\right)$ where $\dot{x}_i = \frac{\mathrm{d}x_i}{\mathrm{d}t}$ and $x_i' = \frac{\partial x_i}{\partial s}$. The resulting equations of motion can be derived using the following equation:

$$\frac{\mathrm{d}}{\mathrm{d}t}\left(\frac{\partial \Lambda}{\partial \dot{x}_i}\right) - \frac{\partial \Lambda}{\partial x_i} + \frac{\mathrm{d}}{\mathrm{d}s}\left(\frac{\partial \Lambda}{\partial x_i'}\right) = 0 \tag{9}$$

where x_i corresponds to w, u, and φ in our system.

The potential energy of this elastic system can be defined as the summation of deformation energy and the work done by the centrifugal force F_{cf}. Using Eq. (7), the potential energy due to the axial strain is

$$U_\varepsilon = \frac{1}{2}\int E\varepsilon_{\mathrm{s}}^2 \mathrm{d}V = \frac{1}{2}\int E\left(u' - z\varphi'\right)^2 \mathrm{d}V = \frac{E}{2}\int_0^L Au'^2 \mathrm{d}s + \frac{E}{2}\int_0^L I\varphi'^2 \mathrm{d}s. \tag{10}$$

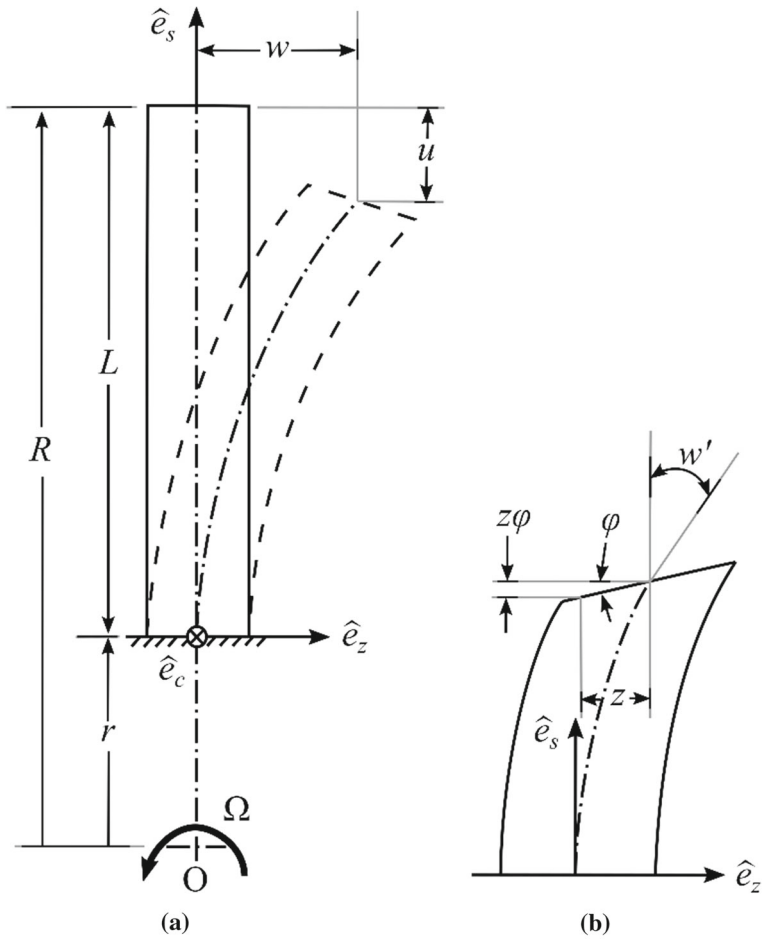

Fig. 3 Schematic diagram of a cantilever Timoshenko beam in a centrifugal force field: **a** axial u and lateral w displacements, and **b** cross-section rotation φ

Using Eq. (8), the potential energy due to shear deformation can be written as

$$U_\gamma = \frac{1}{2}\int kG\gamma_{sz}^2 \mathrm{d}V = \frac{kG}{2}\int_0^L A\left(w' - \varphi\right)^2 \mathrm{d}s \tag{11}$$

where E is Young's modulus and G is shear modulus of the beam material, respectively.

In Eqs. (10) and (11), the cross-section area A and the second area moment of inertia I are functions of the beam span s.

The work done by the centrifugal force F_{cf} can be expressed as

$$U_W = \frac{1}{2}\int_0^L F_{\mathrm{cf}} w'^2 \mathrm{d}s. \tag{12}$$

Noting that the centrifugal force F_{cf} is defined by Eq. (3), the total potential energy can be written as

$$U = U_\varepsilon + U_\gamma + U_W, \tag{13}$$

$$U = \frac{E}{2}\int_0^L Au'^2 \mathrm{d}s + \frac{E}{2}\int_0^L I\varphi'^2 \mathrm{d}s + \frac{kG}{2}\int_0^L A\left(w' - \varphi\right)^2 \mathrm{d}s + \frac{1}{2}\int_0^L F_{\mathrm{cf}} w'^2 \mathrm{d}s. \tag{14}$$

Now, the derivation of the kinetic energy T of the system is discussed. The position vector $\mathbf{r_r}$ of a typical point on the beam at span s and distance z from the midplane in the rotating coordinate system $\left(\hat{e}_z, \hat{e}_s, \hat{e}_c\right)$ can be defined as

$$\mathbf{r_r} = \{w + z, s + u - z\varphi, 0\}^T . \tag{15}$$

The transformation matrix $\mathbf{T}$ used to convert the position vector from a rotating to stationary coordinate systems $(\hat{i}, \hat{j}, \hat{k})$ is defined as

$$\mathbf{T} = \begin{bmatrix} \cos\theta\cos\beta & -\sin\theta & -\cos\theta\sin\beta & -r\sin\theta \\ \sin\theta\cos\beta & \cos\theta & -\sin\theta\sin\beta & r\cos\theta \\ \sin\beta & 0 & \cos\beta & 0 \\ 0 & 0 & 0 & 1 \end{bmatrix} \tag{16}$$

where θ is the rotational angle Ωt.

Using the transformation matrix $\mathbf{T}$, the position vector $\mathbf{r}$ in a stationary coordinate system $\left(\hat{i}, \hat{j}, \hat{k}\right)$ is defined as

$$\mathbf{r} = \left\{ \begin{array}{c} (w + z)\cos\theta\cos\beta - (r + s + u - z\varphi)\sin\theta \\ (w + z)\sin\theta\cos\beta + (r + s + u - z\varphi)\cos\theta \\ (w + z)\sin\beta \end{array} \right\}. \tag{17}$$

Taking the derivative of the position vector $\mathbf{r}$ with respect to time t, we get the velocity vector $\mathbf{v}$ of a typical point of the beam as,

$$\mathbf{v} = \left\{ \begin{array}{c} [\dot{w}\cos\beta - (r + s + u - z\varphi)\,\Omega]\cos\theta - [(\dot{u} - z\dot{\varphi}) + (w + z)\,\Omega\cos\beta]\sin\theta \\ [\dot{w}\cos\beta - (r + s + u - z\varphi)\,\Omega]\sin\theta + [(\dot{u} - z\dot{\varphi}) + (w + z)\,\Omega\cos\beta]\cos\theta \\ \dot{w}\sin\beta \end{array} \right\}. \tag{18}$$

This velocity vector $\mathbf{v}$ gives the resultant velocity which accounts for deformation and rigid body rotation Ω. The kinetic energy of the beam at time t is calculated using

$$T = \int \frac{1}{2} m\,(\mathbf{v}\cdot\mathbf{v})\,\mathrm{d}V = \frac{\rho}{2}\int_0^L A\,(\mathbf{v}\cdot\mathbf{v})\,\mathrm{d}s, \tag{19}$$

$$T = \frac{\rho}{2}\int_0^L A \left[\begin{array}{l} ((\dot{w}\cos\beta - (r + s + u - z\varphi)\,\Omega)\cos\theta - ((\dot{u} - z\dot{\varphi}) + (w + z)\,\Omega\cos\beta)\sin\theta)^2 \\ \quad + ((\dot{w}\cos\beta - (r + s + u - z\varphi)\,\Omega)\sin\theta + ((\dot{u} - z\dot{\varphi}) + (w + z)\,\Omega\cos\beta)\cos\theta)^2 \\ \quad + (\dot{w}\sin\beta)^2 \end{array} \right] \mathrm{d}s. \tag{20}$$

Substituting the kinetic energy (Eq. (20)) and the potential energy (Eq. (14)) expressions in the Lagrangian Λ and solving for the variables w, u, and φ gives the following three equations of motion in terms of w, u and φ:

$$\begin{aligned} &\rho A\frac{\partial^2 w}{\partial t^2} - 2\rho A\Omega\cos\beta\frac{\partial u}{\partial t} - kG\left(A\frac{\partial^2 w}{\partial s^2} + \frac{\partial A}{\partial s}\frac{\partial w}{\partial s}\right) + kG\left(A\frac{\partial \varphi}{\partial s} + \varphi\frac{\partial A}{\partial s}\right) \\ &\quad - \left(F_{\mathrm{cf}}\frac{\partial^2 w}{\partial s^2} + \frac{\partial F_{\mathrm{cf}}}{\partial s}\frac{\partial w}{\partial s}\right) - \rho A\Omega^2\cos^2\beta w = 0, \end{aligned} \tag{21}$$

$$\rho A\frac{\partial^2 u}{\partial t^2} + 2\rho A\Omega\cos\beta\frac{\partial w}{\partial t} - E\left(A\frac{\partial^2 u}{\partial s^2} + \frac{\partial A}{\partial s}\frac{\partial u}{\partial s}\right) - \rho A\Omega^2 u = \rho A\,(r + s)\,\Omega^2, \tag{22}$$

$$\rho I\frac{\partial^2 \varphi}{\partial t^2} - E\left(I\frac{\partial^2 \varphi}{\partial s^2} + \frac{\partial I}{\partial s}\frac{\partial \varphi}{\partial s}\right) - \rho I\Omega^2\varphi - kGA\left(\frac{\partial w}{\partial s} - \varphi\right) = 0. \tag{23}$$

The geometric and natural boundary conditions for the beam can be stated as follows:
The geometric boundary conditions at span $s = 0$:

$$w\,(0, t) = 0, u\,(0, t) = 0,\ \varphi\,(0, t) = 0. \tag{24}$$

The natural boundary conditions at span $s = L$:
Shear force:

$$kAG\left(\frac{\partial w}{\partial s} - \varphi\right) = 0; \tag{25}$$

Axial force:

$$EA\frac{\partial u}{\partial s} = 0; \tag{26}$$

Bending moment:

$$EI\frac{\partial \varphi}{\partial s} = 0; \tag{27}$$

The equations of motion (Eqs. (21)–(23)) are highly nonlinear and coupled. We use the Rayleigh–Ritz method with assumed shape functions to derive the natural frequencies and mode shapes. The assumed shape functions are defined in Eqs. (28)–(30) as follows:

$$w(s,t) = \sum_{j=1}^{n} W_j(s)\, X_j(t) \text{ where } W_j(s) = \frac{1-\cos\left(\alpha_j s\right)}{\alpha_j}, \tag{28}$$

$$u(s,t) = \sum_{j=1}^{n} U_j(s)\, Y_j(t) \text{ where } U_j(s) = \frac{\sin\left(\alpha_j s\right)}{\alpha_j}, \tag{29}$$

$$\varphi(s,t) = \sum_{j=1}^{n} \Phi_j(s)\, Z_j(t) \text{ where } \Phi_j(s) = \sin\left(\alpha_j s\right), \tag{30}$$

and where $\alpha_j = \frac{(2j-1)\pi}{2L}$

These shape functions satisfy the geometric boundary conditions, and the natural boundary conditions are added as force terms in the equations of motion. The variable n is an integer that dictates the number of terms to be used to approximate these functions. The value of the variable n is chosen to be 10 to calculate the first 10 natural frequencies of the beam in each coordinate of w, u, and φ. Applying the Rayleigh–Ritz method to the equations of motion with the assumed shape functions gives the following equations:

$$\begin{aligned}
&\sum_{j=1}^{n}\left[\begin{array}{l}
\rho\left(\sum_{a=0}^{n_A} A_a \int_0^L s^a W_i W_j \mathrm{d}s\right)\ddot{X}_j - 2\rho\Omega\cos\beta\left(\sum_{a=0}^{n_A} A_a \int_0^L s^a W_i U_j \mathrm{d}s\right)\dot{Y}_j \\
\quad - kG\left(\sum_{a=0}^{n_A} A_a \int_0^L s^a W_i W_j'' \mathrm{d}s\right) X_j + kG\left(\sum_{a=0}^{n_A} A_a L^a\right) W_i(L) W_j'(L) X_j \\
\quad - kG\left(\sum_{a=0}^{n_A} a A_a \int_0^L s^{a-1} W_i W_j' \mathrm{d}s\right) X_j \\
\quad - \rho\Omega^2\left(\sum_{a=0}^{n_A} \frac{A_a}{(a+1)(a+2)}\left[L^{a+1}\{(a+1)R + r\}\right]\right)\left(\int_0^L W_i W_j'' \mathrm{d}s\right) X_j \\
\quad + \rho\Omega^2\left(\sum_{a=0}^{n_A} \frac{A_a r}{(a+1)} \int_0^L s^{a+1} W_i W_j \mathrm{d}s\right) X_j + \rho\Omega^2\left(\sum_{a=0}^{n_A} \frac{A_a}{(a+2)} \int_0^L s^{a+2} W_i W_j \mathrm{d}s\right) X_j \\
\quad + \rho\Omega^2\left(\sum_{a=0}^{n_A} A_a r \int_0^L s^a W_i W_j' \mathrm{d}s\right) X_j + \rho\Omega^2\left(\sum_{a=0}^{n_A} A_a \int_0^L s^{a+1} W_i W_j' \mathrm{d}s\right) X_j \\
\quad - \rho\Omega^2\cos^2\beta\left(\sum_{a=0}^{n_A} A_a \int_0^L s^a W_i W_j \mathrm{d}s\right) X_j + kG\left(\sum_{a=0}^{n_A} A_a \int_0^L s^a W_i \Phi_j' \mathrm{d}s\right) Z_j \\
\quad + kG\left(\sum_{a=0}^{n_A} a A_a \int_0^L s^{a-1} W_i \Phi_j \mathrm{d}s\right) Z_j - kG\left(\sum_{a=0}^{n_A} A_a L^a\right) W_i(L)\Phi_j(L) Z_j
\end{array}\right] \\
&= 0,
\end{aligned} \tag{31}$$

$$\begin{aligned}
&\sum_{j=1}^{n}\left[\begin{array}{l}
\rho\left(\sum_{a=0}^{n_A} \int_0^L A_a s^a U_i U_j \mathrm{d}s\right)\ddot{Y}_j + 2\rho\Omega\cos\beta\left(\sum_{a=0}^{n_A} A_a \int_0^L s^a U_i W_j \mathrm{d}s\right)\dot{X}_j \\
\quad - E\left(\sum_{a=0}^{n_A} A_a \int_0^L s^a U_i U_j'' \mathrm{d}s\right) Y_j - E\left(\sum_{a=0}^{n_A} a A_a \int_0^L s^{a-1} U_i U_j' \mathrm{d}s\right) Y_j \\
\quad - \rho\Omega^2\left(\sum_{a=0}^{n_A} A_a \int_0^L s^a U_i U_j \mathrm{d}s\right) Y_j + E\left(\sum_{a=0}^{n_A} A_a L^a\right) U_i(L) U_j'(L) Y_j
\end{array}\right] \\
&= \rho r\Omega^2\left(\sum_{a=0}^{n_A} A_a \int_0^L s^a U_i \mathrm{d}s\right) + \rho\Omega^2\left(\sum_{a=0}^{n_A} A_a \int_0^L s^{a+1} U_i \mathrm{d}s\right),
\end{aligned} \tag{32}$$

$$\sum_{j=1}^{n}\left[\begin{array}{l}\rho\left(\sum_{a=0}^{n_I} I_a\int_0^L s^a\Phi_i\Phi_j\mathrm{d}s\right)\ddot{Z}_j-E\left(\sum_{a=0}^{n_I} I_a\int_0^L s^a\Phi_i\Phi_j''\mathrm{d}s\right)Z_j-E\left(\sum_{a=0}^{n_I} aI_a\int_0^L s^{a-1}\Phi_i\Phi_j'\mathrm{d}s\right)Z_j\\ \quad-\rho\Omega^2\left(\sum_{a=0}^{n_I} I_a\int_0^L s^a\Phi_i\Phi_j\mathrm{d}s\right)Z_j-kG\left(\sum_{a=0}^{n_A} A_a\int_0^L s^a\Phi_iW_j'\mathrm{d}s\right)X_j\\ \quad+kG\left(\sum_{a=0}^{n_A} A_a\int_0^L s^a\Phi_i\Phi_j\mathrm{d}s\right)Z_j\end{array}\right]=0. \tag{33}$$

These equations can be presented in matrix form as follows:

$$\mathbf{M}\left\{\ddot{\xi}\right\}+\mathbf{C}\left\{\dot{\xi}\right\}+\mathbf{K}\left\{\xi\right\}=\{P\} \tag{34}$$

where $\mathbf{M}$, $\mathbf{C}$, and $\mathbf{K}$ are the respective mass, Coriolis damping, and stiffness matrices of size $3n\times 3n$. $\{P\}$ is a force vector of size $3n$, and $\{\xi\}$ is a generalized coordinate vector of size $3n$ composed of X_j, Y_j, and Z_j such that $\{\xi_j\}=X_j$, $\{\xi_{j+n}\}=Y_j$ and $\{\xi_{j+2n}\}=Z_j$. For the purpose of free vibration analysis, the above equation can be written as

$$\mathbf{M}\left\{\ddot{\xi}\right\}+\mathbf{C}\left\{\dot{\xi}\right\}+\left(\mathbf{K^m}+\mathbf{K^\Omega}\right)\{\xi\}=\{0\} \tag{35}$$

where $\mathbf{K^m}$ and $\mathbf{K^\Omega}$ is the elastic property-dependent and the rotational speed-dependent stiffness matrix, respectively.

Equation (35) is solved for eigenvalues to derive the natural frequencies of the beam.

The elements of $\mathbf{M}$, $\mathbf{C}$, $\mathbf{K^m}$, and $\mathbf{K^\Omega}$ are presented in Eqs. (36)–(48) below:

$$\left[M_{i,j}\right]=\rho\left(\sum_{a=0}^{n_A} A_a\int_0^L s^aW_iW_j\mathrm{d}s\right), \tag{36}$$

$$\left[M_{i+n,j+n}\right]=\rho\left(\sum_{a=0}^{n_A} A_a\int_0^L s^aU_iU_j\mathrm{d}s\right), \tag{37}$$

$$\left[M_{i+2n,j+2n}\right]=\rho\left(\sum_{a=0}^{n_I} I_a\int_0^L s^a\Phi_i\Phi_j\mathrm{d}s\right), \tag{38}$$

$$\left[C_{i,j+n}\right]=-2\rho\Omega\cos\beta\left(\sum_{a=0}^{n_A} A_a\int_0^L s^aW_iU_j\mathrm{d}s\right), \tag{39}$$

$$\left[C_{i+n,j}\right]=2\rho\Omega\cos\beta\left(\sum_{a=0}^{n_A} A_a\int_0^L s^aU_iW_j\mathrm{d}s\right), \tag{40}$$

$$\left[K^m_{i,j}\right]=-kG\left[\left(\sum_{a=0}^{n_A} A_a\int_0^L s^aW_iW_j''\mathrm{d}s\right)+\left(\sum_{a=0}^{n_A} aA_a\int_0^L s^{a-1}W_iW_j'\mathrm{d}s\right)-\left(\sum_{a=0}^{n_A} A_aL^a\right)W_i(L)W_j'(L)\right], \tag{41}$$

$$\left[K^m_{i+n,j+n}\right]=-E\left[\left(\sum_{a=0}^{n_A} A_a\int_0^L s^aU_iU_j''\mathrm{d}s\right)+\left(\sum_{a=0}^{n_A} aA_a\int_0^L s^{a-1}U_iU_j'\mathrm{d}s\right)-\left(\sum_{a=0}^{n_A} A_aL^a\right)U_i(L)U_j'(L)\right], \tag{42}$$

$$\left[K^m_{i+2n,j+2n}\right]=kG\left(\sum_{a=0}^{n_A} A_a\int_0^L s^a\Phi_i\Phi_j\mathrm{d}s\right)-E\left[\left(\sum_{a=0}^{n_I} I_a\int_0^L s^a\Phi_i\Phi_j''\mathrm{d}s\right)\right.$$

$$+\left(\sum_{a=0}^{n_I} a I_a \int_0^L s^{a-1}\Phi_i \Phi'_j \mathrm{d}s\right)\Bigg], \tag{43}$$

$$\left[K^m_{i,j+2n}\right] = kG\left[\left(\sum_{a=0}^{n_A} A_a \int_0^L s^a W_i \Phi'_j \mathrm{d}s\right) + \left(\sum_{a=0}^{n_A} a A_a \int_0^L s^{a-1} W_i \Phi_j \mathrm{d}s\right) - \left(\sum_{a=0}^{n_A} A_a L^a\right) W_i(L)\Phi_j(L)\right], \tag{44}$$

$$\left[K^m_{i+2n,j}\right] = -kG\left(\sum_{a=0}^{n_A} A_a \int_0^L s^a \Phi_i W'_j \mathrm{d}s\right), \tag{45}$$

$$\left[K^{\Omega}_{i,j}\right] = -\rho\Omega^2 \begin{bmatrix} \left(\sum_{a=0}^{n_A} \frac{A_a}{(a+1)(a+2)}\left[L^{a+1}\{(a+1)R + r\}\right]\right)\left(\int_0^L W_i W''_j \mathrm{d}s\right) \\ -\left(\sum_{a=0}^{n_A} \frac{A_a r}{(a+1)} \int_0^L s^{a+1} W_i W''_j \mathrm{d}s\right) - \left(\sum_{a=0}^{n_A} \frac{A_a}{(a+2)} \int_0^L s^{a+2} W_i W''_j \mathrm{d}s\right) \\ -\left(\sum_{a=0}^{n_A} A_a r \int_0^L s^a W_i W'_j \mathrm{d}s\right) - \left(\sum_{a=0}^{n_A} A_a \int_0^L s^{a+1} W_i W'_j \mathrm{d}s\right) \\ +\cos^2\beta \left(\sum_{a=0}^{n_A} A_a \int_0^L s^a W_i W_j \mathrm{d}s\right) \end{bmatrix}, \tag{46}$$

$$\left[K^{\Omega}_{i+n,j+n}\right] = -\rho\Omega^2 \left(\sum_{a=0}^{n_A} A_a \int_0^L s^a U_i U_j \mathrm{d}s\right), \tag{47}$$

$$\left[K^{\Omega}_{i+2n,j+2n}\right] = -\rho\Omega^2 \left(\sum_{a=0}^{n_I} I_a \int_0^L s^a \Phi_i \Phi_j \mathrm{d}s\right). \tag{48}$$

3 Results and discussion

The above analytical model is used to analyze the effect of hub radius, taper ratio, slenderness ratio, chord ratio, and rotational speed on the lateral and axial natural frequencies of the beam. A typical gas turbine engine (GTE) blade made of Ti6Al4V is considered for the purpose of the analysis. The relevant parameters of the beam are presented in Table 1.

The non-dimensional parameters used to define the beam properties are presented in Table 2, where h_R and h_r are thickness of the beam at the tip and hub, respectively, as shown in Fig. 4. The chord length (width) of the beam at the tip and hub are c_R and c_r, respectively. The cross-section area of the beam at the hub, second moment of inertia of the beam at the hub, and natural frequency in rad/s are A_r, I_r, and ω_n, respectively.

The following Sections present results for the two cases of tapered beams: (i) linearly tapered beams and (ii) exponentially tapered beams. The linear variations in the thickness and chord length (width) of the beams can be defined by Eqs. (49) and (50), respectively,

$$h(s) = h_r\left(1 - \bar{h}\right), \tag{49}$$

Table 1 Geometric and material properties of the beam

Density, ρ	4466 kg/m^3
Young's modulus, E	117 GPa
Poisson's ratio, ν	0.3
Shear coefficient, k	0.833
Length of the beam, L	1 m
Chord length at the hub, c_r	0.25 m
Stagger angle, β	0°

Table 2 Non-dimensional parameters of the beam

Non-dimensional hub radius, $\bar{r}$	$\frac{r}{L}$
Taper ratio, $\bar{h}$	$1-\frac{h_R}{h_r}$
Chord ratio, $\bar{c}$	$1-\frac{c_R}{c_r}$
Slenderness ratio, $\bar{d}$	$\sqrt{\frac{I_r}{A_r L^2}}$
Non-dimensional rotational speed, $\bar{\Omega}$	$\Omega\left(\frac{\rho A_r L^4}{E I_r}\right)$
Non-dimensional natural frequency, $\bar{\omega}_n$	$\omega_n\left(\frac{\rho A_r L^4}{E I_r}\right)$

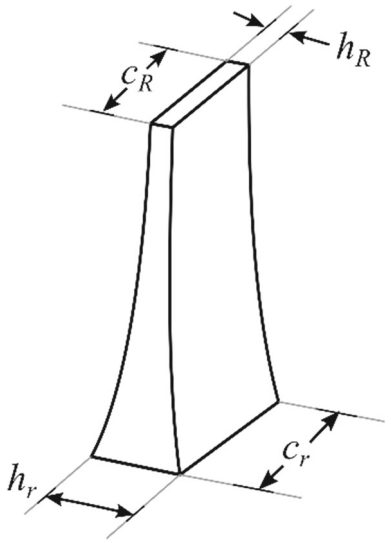

Fig. 4 Representation of thickness and chord length (width) of the beam at the hub and tip

$$c\,(s) = c_r\,(1-\bar{c})\,. \tag{50}$$

where $h\,(s)$ and $c\,(s)$ are the thickness and chord length of the beam at span s.

The exponential variations in the thickness and chord length (width) of beams can be defined by Eqs. (51) and (52), respectively,

$$h\,(s) = h_r e^{\ln(1-\bar{h})\frac{s}{L}}, \tag{51}$$

$$c\,(s) = c_r e^{\ln(1-\bar{c})\frac{s}{L}}. \tag{52}$$

The resulting variations in the cross-section area and moment of inertia are converted in the polynomial form as defined in Eqs. (1) and (2), to allow their use in the analytical formulation. The presented formulation is programmed using C++ to derive the solution for the free vibration response. Some of the important results are presented below.

3.1 Effect of Coriolis coupling

The coupling of axial and lateral displacement due to the Coriolis effect can be identified by the terms $-2\rho A\Omega\cos\beta\frac{\partial u}{\partial t}$ and $+2\rho A\Omega\cos\beta\frac{\partial w}{\partial t}$ in the equations of motion (Eqs. (21)–(23)). These terms appear as a skew-symmetric damping matrix $\mathbf{C}$ in the matrix form of the equations of motion (Eq. (35)). In this Section, the results of natural frequencies derived from Eq. (35) are compared with the case where the Coriolis damping matrix $\mathbf{C}$ is ignored. The comparison of the results for both linearly and exponentially tapered beams at rotational speed $\bar{\Omega} = 2$, 6 and 10 is shown in Tables 3 and 4, respectively. The other parameters of the beam are kept constant at $\bar{r} = 0.5$, $\bar{h} = 0.5$, $\bar{c} = 0$, and $\bar{d} = 0.025$. Coriolis coupling has an insignificant effect on both axial and lateral natural frequencies. The first natural frequencies show a maximum difference of about 4% for $\bar{\Omega}$ =

Table 3 Lateral and axial natural frequencies of a linearly tapered beam with and without Coriolis coupling ($\bar{r} = 0.5$, $\bar{h} = 0.5$, $\bar{c} = 0$ and $\bar{d} = 0.025$)

$\bar{\Omega}$	Lateral natural frequency						Axial natural frequency					
	2		6		10		2		6		10	
	With coupling	Without coupling	With coupling	Without coupling	With coupling	Without coupling	With coupling	Without coupling	With coupling	Without coupling	With coupling	Without coupling
$\bar{\omega}_1$	4.333	4.339	7.050	7.144	10.105	10.488	71.844	71.733	72.523	71.509	73.916	71.061
$\bar{\omega}_2$	18.812	18.818	24.891	24.953	33.748	33.968	192.116	192.072	192.356	191.989	192.909	191.823
$\bar{\omega}_3$	45.908	45.914	53.145	53.198	65.021	65.210	316.382	316.352	316.522	316.302	316.857	316.201
$\bar{\omega}_4$	83.994	83.997	92.073	92.110	106.177	106.308	441.419	441.400	441.533	441.364	441.777	441.292
$\bar{\omega}_5$	131.162	131.166	139.907	139.947	155.727	155.855	566.732	566.717	566.820	566.689	567.005	566.633

Table 4 Lateral and axial natural frequencies of an exponentially tapered beam with and without Coriolis coupling ($\bar{r} = 0.5$,$\bar{h} = 0.5$, $\bar{c} = 0$ and $\bar{d} = 0.025$)

$\bar{\Omega}$	Lateral natural frequency						Axial natural frequency					
	2		6		10		2		6		10	
	With coupling	Without coupling	With coupling	Without coupling	With coupling	Without coupling	With coupling	Without coupling	With coupling	Without coupling	With coupling	Without coupling
$\bar{\omega}_1$	4.239	4.245	7.017	7.110	10.091	10.472	72.020	71.909	72.695	71.687	74.080	71.239
$\bar{\omega}_2$	18.150	18.156	24.470	24.530	33.527	33.743	191.923	191.880	192.217	191.796	152.496	152.621
$\bar{\omega}_3$	44.290	44.295	51.833	51.884	64.066	64.247	316.239	316.212	316.058	316.162	316.712	316.060
$\bar{\omega}_4$	81.172	81.175	89.591	89.627	104.162	104.291	441.313	441.295	441.427	441.258	441.668	441.186
$\bar{\omega}_5$	127.042	127.047	136.139	136.177	192.713	191.630	566.648	566.634	566.737	566.606	566.922	566.550

10, and all other natural frequencies show a variation of less than 1%. However, for the sake of completeness, all the results presented after here take into account the effect of coupling due to the damping matrix **C**.

3.2 Validation of the model

The validity of the present analytical model is ascertained by comparing the natural frequencies of a much simplified case involving a linearly tapered beam with the results from finite element analysis using the commercial code ANSYS. The finite element model uses tapered beam elements whose motion is restricted in the XY plane only and subjected to rotational speed about the Z axis as shown in Fig. 5. The beam is assumed to have hub radius $\bar{r} = 0.5$, chord ratio $\bar{c} = 0.5$, slenderness ratio $\bar{d} = 0.025$, and non-dimensional rotational speed $\bar{\Omega} = 5$. The first five computed natural frequencies are compared for linearly tapered beams with taper ratio $\bar{h} = 0.4$ and 0.8, and presented in Table 5. The results are found to be in good agreement with each other.

Commercial FE codes have only the linearly tapered Timoshenko beam formulation and do not allow direct modeling of an exponential taper in the beams. However, for the purpose of validation, the nonlinear exponentially tapered beam geometry is modeled by approximating it as a number of linearly tapered beams in ANSYS. The first five computed natural frequencies are compared for taper ratio $\bar{h} = 0.4$ and 0.8 and presented in Table 6. The results are found to be in good agreement, except that the higher-order lateral natural frequencies for $\bar{h} = 0.8$ show a difference of about 8%. This is due to the approximation of the nonlinear tapered beam by a number of linearly tapered beams in the FE model. These results also highlight the advantages of the present analytical model over commercial FE codes in accurately accounting for the nonlinearities in the beam geometry.

3.3 Effect of taper ratio and rotational speed

In this Section, the effects of the taper ratio $\bar{h}$ and the rotational speed $\bar{\Omega}$ on the free vibration response of linearly and exponentially tapered beams are presented. The other parameters of the beam are kept constant at $\bar{r} = 0.5$, $\bar{c} = 0$, and $\bar{d} = 0.025$. Figures 6 and 7 depict the variation in lateral natural frequencies for

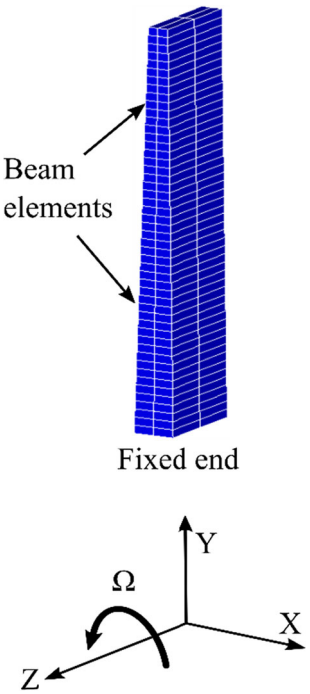

Fig. 5 Finite element model of a rotating tapered beam

Table 5 Lateral and axial natural frequencies of a linearly tapered beam ($\bar{r} = 0.5$, $\bar{c} = 0.5$, $\bar{d} = 0.025$ and $\bar{\Omega} = 5$)

$\bar{h}$	Lateral natural frequency				Axial natural frequency			
	0.4		0.8		0.4		0.8	
	Present	FEM	Present	FEM	Present	FEM	Present	FEM
$\bar{\omega}_1$	6.829	6.880	7.557	7.600	79.186	78.849	92.469	92.186
$\bar{\omega}_2$	24.304	24.219	21.165	21.182	195.411	195.778	205.057	205.279
$\bar{\omega}_3$	54.227	53.615	42.137	42.100	318.427	319.266	325.200	325.817
$\bar{\omega}_4$	95.635	94.032	71.359	71.160	442.905	444.159	427.873	448.967
$\bar{\omega}_5$	146.250	143.390	108.275	107.756	567.892	569.543	572.005	569.151

linearly and exponentially tapered beams, respectively. The first lateral natural frequency shows an increasing trend with the increase in $\bar{h}$, whereas the other four frequencies show reducing trends. The effect of the taper ratio $\bar{h}$ is more significant for the higher-order lateral natural frequencies. For example, for a linearly tapered beam with $\bar{\Omega} = 5$, the first natural frequency increases by 16%, and the fifth natural frequency decreases by 36% with the change in $\bar{h}$ from 0 to 0.8. The rotational speed $\bar{\Omega}$ also has a significant effect on the lateral natural frequencies of the beam. However, the effect of rotational speed $\bar{\Omega}$ is less significant for higher-order frequencies, as shown in Figs. 6 and 7. For a linearly tapered beam with $\bar{h} = 0.4$, the first natural frequency increases by 2.8 times, but the fifth natural frequency increases by 1.2 with a change in $\bar{\Omega}$ from 0 to 10.

The results of lateral vibrations of linearly and exponentially tapered beams for $\bar{\Omega} = 10$ are compared in Fig. 8 to show the effect of nonlinearities in the cross section on the natural frequencies. If curve-fit lines are used, the variations in lateral natural frequencies for the linearly tapered beam can be identified by a second-order polynomial. Because of highly nonlinear cross-section properties of an exponentially tapered beam, it requires a fourth-order polynomial to accurately represent the results. Furthermore, the difference in their results increases with increase in $\bar{h}$ with 12% difference between linearly and exponentially tapered beams with $\bar{h} = 0.8$.

Table 7 shows the axial natural frequency results with a change in $\bar{h}$ and $\bar{\Omega}$. All axial natural frequencies are found to be increasing with the increase in $\bar{h}$. However, the effect of the taper ratio $\bar{h}$ becomes less significant for higher-order frequencies. The rotational speed $\bar{\Omega}$ has a little effect on the axial natural frequencies. Changing $\bar{\Omega}$ from 0 to 5 changes the first axial natural frequency by 0.3% for both linearly and exponentially tapered beams with $\bar{h} = 0.4$.

Table 6 Lateral and axial natural frequencies of an exponentially tapered beam ($\bar{r} = 0.5$, $\bar{c} = 0.5$, $\bar{d} = 0.025$ and $\bar{\Omega} = 5$)

$\bar{h}$	Lateral natural frequency				Axial natural frequency			
	0.4		0.8		0.4		0.8	
	Present	FEM	Present	FEM	Present	FEM	Present	FEM
$\bar{\omega}_1$	6.806	6.856	7.264	7.302	79.461	79.124	92.469	95.397
$\bar{\omega}_2$	23.919	23.932	19.079	19.197	195.135	195.503	205.057	203.201
$\bar{\omega}_3$	52.891	52.795	34.492	36.734	318.218	319.060	325.200	323.209
$\bar{\omega}_4$	93.029	92.569	56.418	61.050	442.746	444.002	427.873	446.323
$\bar{\omega}_5$	142.276	141.249	85.946	91.955	567.767	569.445	572.005	570.552

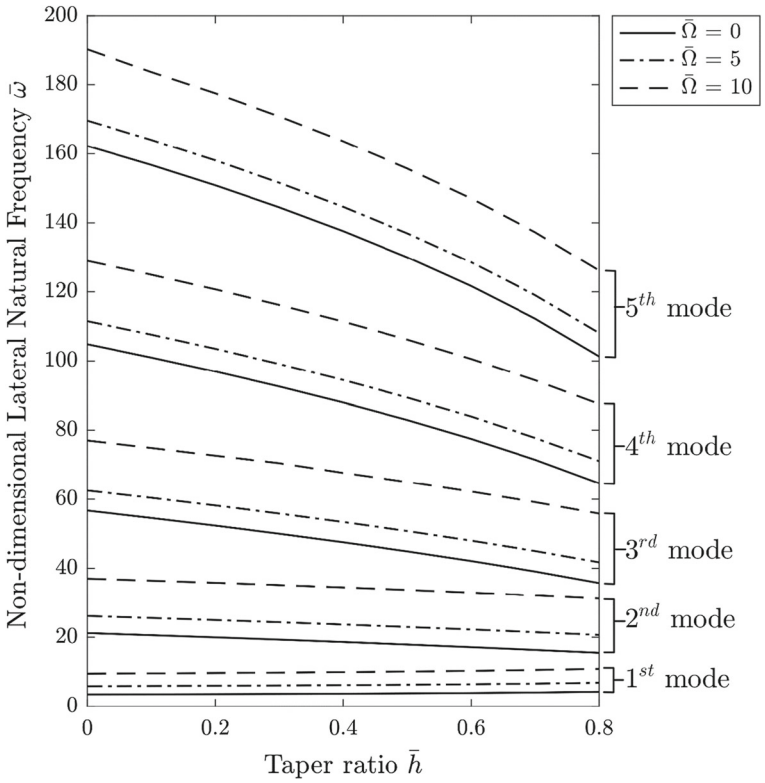

Fig. 6 Variation of lateral natural frequencies with taper ratio and rotational speed for linearly tapered beams ($\bar{r} = 0.5$, $\bar{c} = 0$ and $\bar{d} = 0.025$)

3.4 Effect of chord ratio

In this Section, we examine the effect of the chord ratio $\bar{c}$ on the free vibration of linearly and exponentially tapered beams with the following parameters being kept constant: $\bar{r} = 0.5$, $\bar{h} = 0.5$ $\bar{d} = 0.025$, and $\bar{\Omega} = 5$. The variations of the lateral and the axial natural frequencies with $\bar{c}$ are presented in Tables 8 and 9, respectively. Both, the lateral and the axial natural frequencies, increase with the increase in $\bar{c}$. The first natural frequency is significantly affected by $\bar{c}$, but the effect of $\bar{c}$ reduces for the higher-order natural frequencies. For example, the first lateral natural frequency changes by 24% for a change in $\bar{c}$ from 0 to 0.8. However, the fifth lateral natural frequency changes by a mere 0.6%.

3.5 Effect of hub radius

In this case, we changed the hub radius $\bar{r}$ and kept the length of the beam constant at 1 m such that $\bar{r}$ would vary from 0 to 1. For this analysis, the other non-dimensional parameters were kept constant at $\bar{h} = 0.5$, $\bar{c} = 0$, $\bar{d} = 0.025$, and $\bar{\Omega} = 5$. The results of the first five lateral natural frequencies are presented in Table 10. The

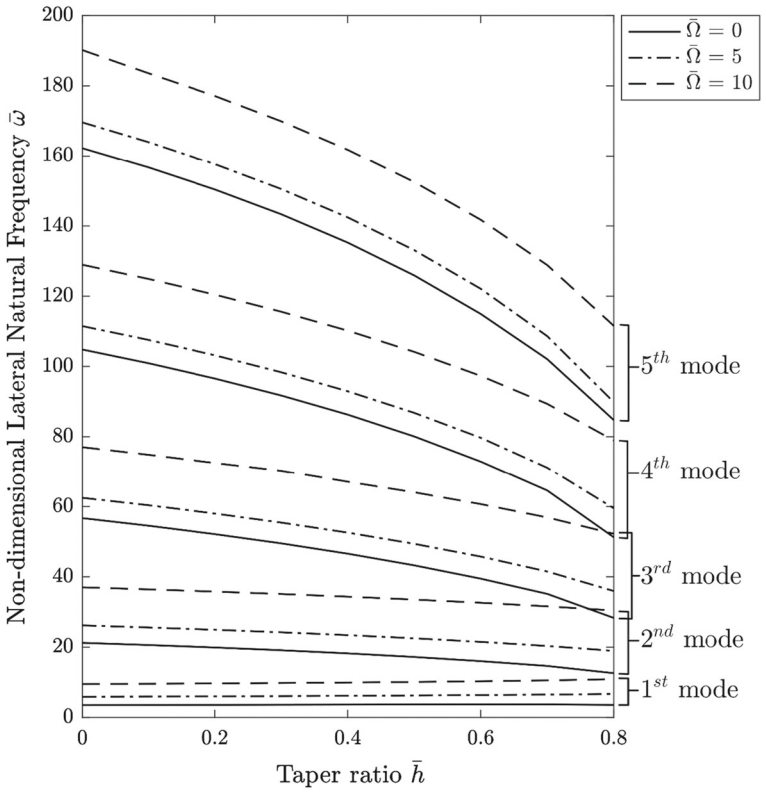

Fig. 7 Variation of lateral natural frequencies with taper ratio and rotational speed for exponentially tapered beams ($\bar{r} = 0.5$, $\bar{c} = 0$ and $\bar{d} = 0.025$)

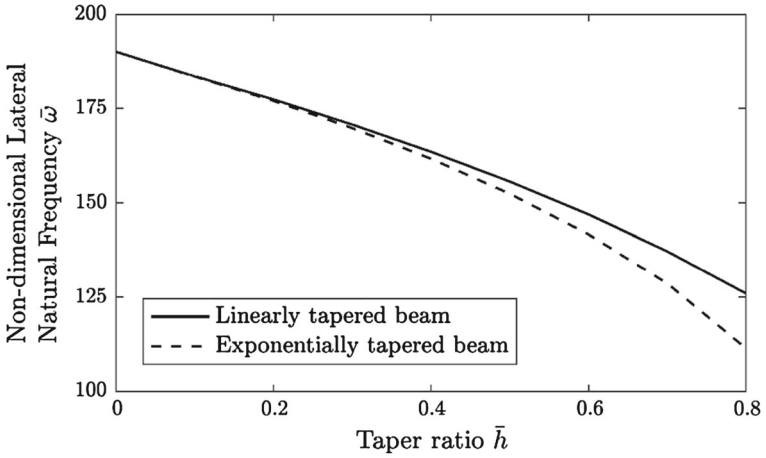

Fig. 8 Comparison of fifth lateral natural frequency results of linearly and exponentially tapered beams ($\bar{r} = 0.5, \bar{c} = 0, \bar{d} = 0.025$ and $\bar{\Omega} = 10$)

lateral natural frequencies are found to increase with an increase in $\bar{r}$. However, the effect of $\bar{r}$ reduces for the higher-order frequencies. For example, for a linearly tapered beam, the first natural frequency increases by 73% with an increase in $\bar{r}$ from 0 to 1, but the increase in the fifth natural frequency is only 4%. The values of the lateral natural frequencies are found to be close to each other for linearly and exponentially tapered beams for $\bar{h} = 0.5$.

Table 11 shows results of the first five axial natural frequencies for both linearly and exponentially tapered beams. All natural frequencies are found to have very small variations with the change in $\bar{r}$. These results are due to the fact that the corresponding terms relating to axial motion in the stiffness matrix

Table 7 Variation of axial natural frequencies with taper ratio and rotational speed ($\bar{r} = 0.5$, $\bar{c} = 0$, and $\bar{d} = 0.025$)

$\bar{h}$	Linearly tapered beam					Exponentially tapered beam				
	$\bar{\omega}_1$	$\bar{\omega}_2$	$\bar{\omega}_3$	$\bar{\omega}_4$	$\bar{\omega}_5$	$\bar{\omega}_1$	$\bar{\omega}_2$	$\bar{\omega}_3$	$\bar{\omega}_4$	$\bar{\omega}_5$
$\bar{\Omega} = 0$										
0	62.832	188.496	314.159	439.822	565.486	62.832	188.496	314.159	439.822	565.486
0.2	65.697	189.497	314.763	440.254	565.823	65.703	189.490	314.758	440.251	565.821
0.4	69.421	190.990	315.676	440.912	566.336	69.489	190.912	315.620	440.870	566.302
0.6	74.560	193.594	317.332	442.116	567.280	74.982	193.169	317.004	441.865	567.079
0.8	82.356	199.452	321.536	445.330	569.866	84.759	197.689	319.807	443.889	568.660
$\bar{\Omega} = 5$										
0	63.502	188.708	314.283	439.903	565.563	63.502	188.708	314.283	439.903	565.563
0.2	66.283	189.703	314.885	440.355	565.893	66.288	189.696	314.880	440.349	565.891
0.4	69.969	191.190	315.795	441.000	566.404	70.036	191.110	315.738	440.959	566.371
0.6	75.063	193.796	317.458	442.201	567.349	75.473	193.369	317.128	441.958	567.147
0.8	82.822	199.628	321.653	445.420	569.934	85.204	197.887	319.931	443.978	568.730

Table 8 Variation of lateral natural frequencies with chord ratio ($\bar{r} = 0.5$, $\bar{h} = 0.5$, $\bar{d} = 0.025$, and $\bar{\Omega} = 5$)

$\bar{c}$	Linearly tapered beam					Exponentially tapered beam				
	$\bar{\omega}_1$	$\bar{\omega}_2$	$\bar{\omega}_3$	$\bar{\omega}_4$	$\bar{\omega}_5$	$\bar{\omega}_1$	$\bar{\omega}_2$	$\bar{\omega}_3$	$\bar{\omega}_4$	$\bar{\omega}_5$
0	6.293	22.993	50.786	89.391	136.973	6.251	22.511	49.384	86.802	133.093
0.2	6.497	23.135	50.866	89.398	136.914	6.447	22.636	49.447	86.792	133.012
0.4	6.770	23.339	51.010	89.470	136.908	6.716	22.835	49.573	86.834	132.966
0.6	7.175	23.692	51.318	89.717	137.063	7.130	23.174	49.834	87.011	132.996
0.8	7.849	24.505	52.210	90.532	137.859	7.928	23.922	50.453	87.341	133.114

Table 9 Variation of axial natural frequencies with chord ratio ($\bar{r} = 0.5$ $\bar{h} = 0.5$, $\bar{d} = 0.025$, and $\bar{\Omega} = 5$)

$\bar{c}$	Linearly tapered beam					Exponentially tapered beam				
	$\bar{\omega}_1$	$\bar{\omega}_2$	$\bar{\omega}_3$	$\bar{\omega}_4$	$\bar{\omega}_5$	$\bar{\omega}_1$	$\bar{\omega}_2$	$\bar{\omega}_3$	$\bar{\omega}_4$	$\bar{\omega}_5$
0	72.288	192.136	316.462	441.493	566.790	72.463	192.100	316.361	441.387	566.7061
0.2	75.296	193.598	317.243	442.065	567.235	75.484	193.376	317.142	441.953	567.147
0.4	79.183	195.427	318.358	442.903	567.892	79.456	195.149	318.236	442.745	567.767
0.6	84.498	198.498	320.483	444.371	569.047	85.175	197.890	319.938	443.976	568.730
0.8	92.509	205.028	325.215	448.038	572.005	87.341	203.230	323.235	446.338	570.566

Table 10 Variation of lateral natural frequencies with hub radius ($\bar{h} = 0.5$, $\bar{c} = 0$, $\bar{d} = 0.025$, and $\bar{\Omega} = 5$)

$\bar{r}$	Linearly tapered beam					Exponentially tapered beam				
	$\bar{\omega}_1$	$\bar{\omega}_2$	$\bar{\omega}_3$	$\bar{\omega}_4$	$\bar{\omega}_5$	$\bar{\omega}_1$	$\bar{\omega}_2$	$\bar{\omega}_3$	$\bar{\omega}_4$	$\bar{\omega}_5$
0	4.445	20.876	48.371	86.711	134.066	4.384	20.324	46.879	84.022	130.084
0.2	5.264	21.749	49.353	87.794	135.238	5.213	21.227	47.899	85.147	131.297
0.4	5.971	22.586	50.313	88.862	136.398	5.926	22.091	48.895	86.254	132.497
0.6	6.599	23.393	51.254	89.916	137.546	6.559	22.922	49.869	87.345	133.686
0.8	7.173	24.170	52.175	90.954	138.683	7.135	23.721	50.821	88.422	134.860
1	7.702	24.923	53.079	91.980	139.809	7.667	24.493	51.755	89.483	136.025

$-\rho\Omega^2 \left(\sum_{a=0}^{n_A} A_a \int_0^L s^a U_i U_j \mathrm{d}s\right)$ (in Eq. (31)) are independent of the hub radius r. The small variations are observed only due to coupling of the lateral and axial displacements due to the Coriolis effect.

3.6 Effect of slenderness ratio

Contrary to the effect of other parameters, the slenderness ratio $\bar{d}$ plays a dramatic role for the axial natural frequencies of the beam, as depicted in Fig. 9. All five axial natural frequencies show a decrease of 10 times for a change in $\bar{d}$ from 0.005 to 0.05. The lateral natural frequencies show a decreasing trend with the increase in

Table 11 Variation of axial natural frequencies with hub radius ($\bar{h} = 0.5$, $\bar{c} = 0$, $\bar{d} = 0.025$ and $\bar{\Omega} = 5$)

$\bar{r}$	Linearly tapered beam					Exponentially tapered beam				
	$\bar{\omega}_1$	$\bar{\omega}_2$	$\bar{\omega}_3$	$\bar{\omega}_4$	$\bar{\omega}_5$	$\bar{\omega}_1$	$\bar{\omega}_2$	$\bar{\omega}_3$	$\bar{\omega}_4$	$\bar{\omega}_5$
0	72.284	192.297	316.241	441.493	566.789	72.457	192.095	316.351	441.386	566.706
0.2	72.285	192.307	316.434	441.493	566.789	72.459	192.097	316.353	441.386	566.706
0.4	72.288	192.360	316.456	441.493	566.790	72.461	192.099	316.358	441.387	566.706
0.6	72.289	192.232	316.465	441.493	566.790	72.463	192.102	316.367	441.387	566.706
0.8	72.291	192.263	316.470	441.494	566.790	72.465	192.106	316.390	441.387	566.706
1	72.293	192.272	316.472	441.494	566.790	72.467	192.117	316.581	441.388	566.707

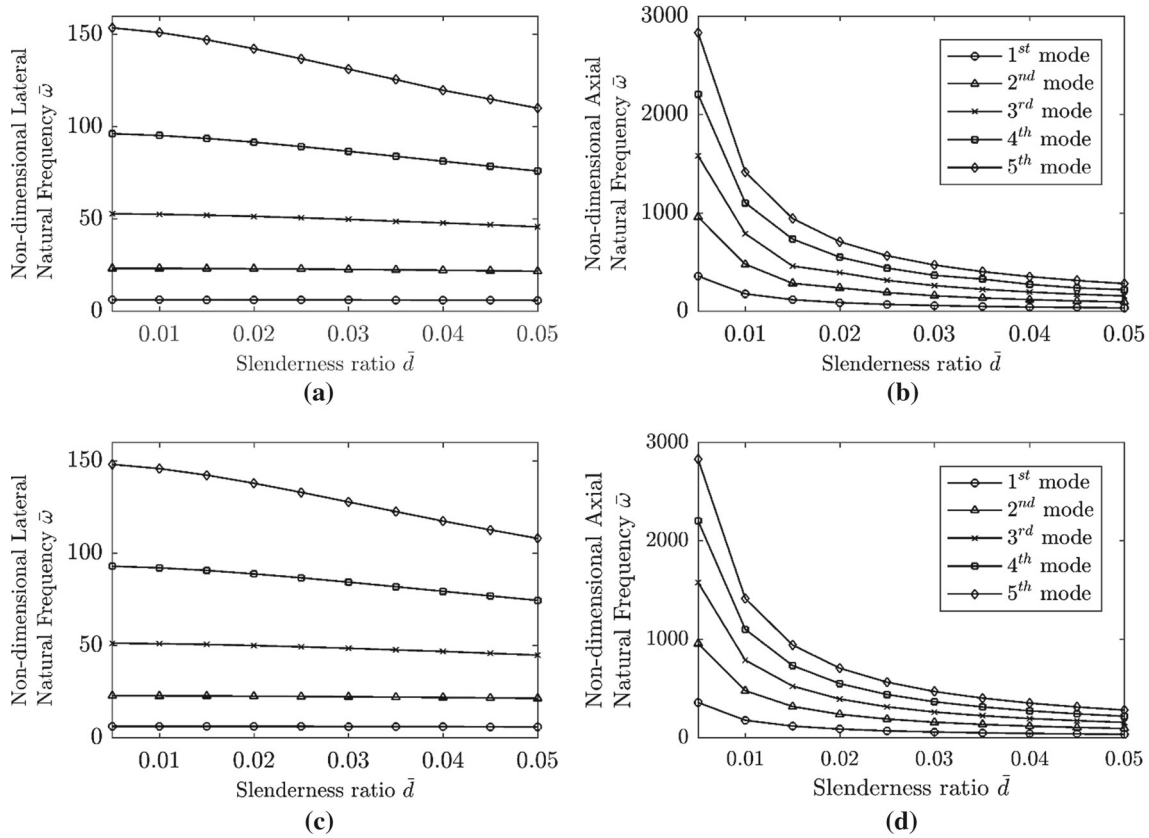

Fig. 9 Variation of **a** lateral and **b** axial natural frequencies of linearly tapered beams, and **c** lateral and **d** axial natural frequencies of exponentially tapered beams with slenderness ratio ($\bar{h} = 0.5$, $\bar{c} = 0$, $\bar{r} = 0.5$ and $\bar{\Omega} = 5$)

$\bar{d}$. However, the effect is not as severe as observed in the axial vibration case. The first lateral natural frequency for exponentially tapered beams shows a change of 2% with the change in $\bar{d}$ from 0.005 to 0.05. However, the fifth lateral natural frequency shows a significant change of 27%.

4 Conclusions

This paper considers the free vibration response of a rotating Timoshenko beam with nonlinear variations in the cross-section properties, taking into account the coupling between the axial and the lateral displacements, shear deformation, rotary inertia, and change in stiffness due to rotational speed. The governing equations of motion are derived using Lagrangian mechanics. These equations are solved using the Rayleigh–Ritz method leading to the axial and lateral natural frequencies of the beam. A parametric study is performed to analyze the effect of hub radius, chord ratio, taper ratio, slenderness ratio, and rotational speed on the free vibration of the beam. Given below is a summary of our findings:

(i) The first lateral natural frequency increases with the increase in the taper ratio, while the other lateral natural frequencies exhibit a decreasing trend. All axial natural frequencies increase with the increase in the taper ratio.
(ii) The rotational speed plays a significant role for the lateral vibration modes and results in an increase in the lateral frequencies. However, it plays an insignificant role for the axial natural frequencies.
(iii) The lateral natural frequencies increase with the increase in the hub radius and chord ratio. However, the axial natural frequencies are found to be independent of the hub radius.
(iv) Both lateral and axial natural frequencies decrease with the increase in the slenderness ratio. The axial natural frequencies show a significant decrease by an order of magnitude with the increase in the taper ratio.

Acknowledgements The authors wish to acknowledge the Natural Sciences and Engineering Research Council (NSERC) for their kind support of these studies.

Funding Funding for this project was provided by NSERC under an operating Grant # 48568/2013-2017 for the senior author (SAM).

References

1. Hodges, D.H., Rutkowskij, M.J.: Free-vibration analysis of rotating beams by a variable-order finite-element method. AIAA J. **19**, 1459–1466 (1981). https://doi.org/10.2514/3.60082
2. Wang, X., Shi, J.: Validation of Johnson–Cook plasticity and damage model using impact experiment. Int. J. Impact Eng. **60**, 67–75 (2013). https://doi.org/10.1016/j.ijimpeng.2013.04.010
3. Bazoune, A.: Effect of tapering on natural frequencies of rotating beams. Shock Vib. **14**, 169–179 (2007). https://doi.org/10.1155/2007/865109
4. Zhou, D., Cheung, Y.K.: The free vibration of a type of tapered beams. Comput. Methods Appl. Mech. Eng. **188**, 203–216 (2000). https://doi.org/10.1016/S0045-7825(99)00148-6
5. Ece, M.C., Aydogdu, M., Taskin, V.: Vibration of a variable cross-section beam. Mech. Res. Commun. **34**, 78–84 (2007). https://doi.org/10.1016/j.mechrescom.2006.06.005
6. Mao, Q., Pietrzko, S.: Free vibration analysis of a type of tapered beams by using Adomian decomposition method. Appl. Math. Comput. **219**, 3264–3271 (2012). https://doi.org/10.1016/j.amc.2012.09.069
7. Kane, T.R., Ryan, R.R., Banerjee, A.K.: Dynamics of a cantilever beam attached to a moving base. J. Guid. Control. Dyn. **12**, 139–151 (1987). https://doi.org/10.2514/3.20195
8. Khulief, Y.A.: Vibration frequencies of a rotating tapered beam with end mass. J. Sound Vib. **134**, 87–97 (1989). https://doi.org/10.1016/0022-460X(89)90738-4
9. Naguleswaran, S.: Lateral vibration of a centrifugally tensioned uniform Euler–Bernoulli beam. J. Sound Vib. **176**, 613–624 (1994). https://doi.org/10.1006/jsvi.1994.1402
10. Yang, J.B., Jiang, L.J., Chen, D.C.: Dynamic modelling and control of a rotating Euler–Bernoulli beam. J. Sound Vib. **274**, 863–875 (2004). https://doi.org/10.1016/S0022-460X(03)00611-4
11. Banerjee, J.R., Su, H.: Development of a dynamic stiffness matrix for free vibration analysis of spinning beams. Comput. Struct. **82**, 2189–2197 (2004). https://doi.org/10.1016/j.compstruc.2004.03.058
12. Banerjee, J.R., Su, H., Jackson, D.R.: Free vibration of rotating tapered beams using the dynamic stiffness method. J. Sound Vib. **298**, 1034–1054 (2006). https://doi.org/10.1016/j.jsv.2006.06.040
13. Wang, G., Wereley, N.M.: Free vibration analysis of rotating blades with uniform tapers. AIAA J. **42**, 2429–2437 (2004). https://doi.org/10.2514/1.4302
14. Ozgumus, O.O., Kaya, M.O.: Flapwise bending vibration analysis of double tapered rotating Euler–Bernoulli beam by using the differential transform method. Meccanica **41**, 661–670 (2006). https://doi.org/10.1007/s11012-006-9012-z
15. Attarnejad, R., Shahba, A.: Dynamic basic displacement functions in free vibration analysis of centrifugally stiffened tapered beams. A mechanical solution. Meccanica **46**, 1267–1281 (2011). https://doi.org/10.1007/s11012-010-9383-z
16. Firouz-abadi, R.D., Haddadpour, H., Novinzadeh, A.B.: An asymptotic solution to transverse free vibrations of variable-section beams. J. Sound Vib. **304**, 530–540 (2007). https://doi.org/10.1016/j.jsv.2007.02.030
17. Lee, J.W., Lee, J.Y.: Free vibration analysis using the transfer-matrix method on a tapered beam. Comput. Struct. **164**, 75–82 (2016). https://doi.org/10.1016/j.compstruc.2015.11.007
18. Vinod, K.G., Gopalakrishnan, S., Ganguli, R.: Free vibration and wave propagation analysis of uniform and tapered rotating beams using spectrally formulated finite elements. Solids Struct. **44**, 5875–5893 (2007). https://doi.org/10.1016/j.ijsolstr.2007.02.002
19. Fung, E.H.K., Yau, D.T.W.: Effects of centrifugal stiffening on the vibration frequencies of a constrained flexible arm. J. Sound Vib. **224**, 809–841 (1999). https://doi.org/10.1006/jsvi.1999.2212
20. Huang, C.L., Lin, W.Y., Hsiao, K.M.: Free vibration analysis of rotating Euler beams at high angular velocity. Comput. Struct. **88**, 991–1001 (2010). https://doi.org/10.1016/j.compstruc.2010.06.001
21. Liao, C.-L., Huang, B.-W.: Parametric instability of a spinning pretwisted beam under periodic axial force. Int. J. Mech. Sci. **37**, 423–439 (1994). https://doi.org/10.1017/CBO9781107415324.004
22. Sarkar, K., Ganguli, R.: Closed-form solutions for non-uniform Euler–Bernoulli free-free beams. J. Sound Vib. **332**, 6078–6092 (2013). https://doi.org/10.1016/j.jsv.2013.06.008
23. Weaver Jr., W., Timoshenko, S.P., Young, D.H.: Vibration problems in engineering. Wiley, New York (1990)

24. Lee, S.Y., Lint, S.M.: Exact vibration solutions for nonuniform Timoshenko beams with attachments. AIAA J. **30**, 2930–2934 (1992). https://doi.org/10.2514/3.48979
25. Auciello, N.M., Ercolano, A.: A general solution for dynamic response of axially loaded non-uniform Timoshenko beams. Int. J. Solids Struct. **41**, 4861–4874 (2004). https://doi.org/10.1016/j.ijsolstr.2004.04.036
26. Yuan, S., Ye, K., Xiao, C., Williams, F.W., Kennedy, D.: Exact dynamic stiffness method for non-uniform Timoshenko beam vibrations and Bernoulli–Euler column buckling. J. Sound Vib. **303**, 526–537 (2007). https://doi.org/10.1016/j.jsv.2007.01.036
27. Ozgumus, O.O., Kaya, M.O.: Vibration analysis of a rotating tapered Timoshenko beam using DTM. Meccanica **45**, 33–42 (2010). https://doi.org/10.1007/s11012-009-9221-3
28. Zhou, D., Cheung, Y.K.: Vibrations of tapered Timoshenko beam in terms of static Timoshenko beam functions. J. Appl. Mech. **68**, 596–602 (2001). https://doi.org/10.1115/1.1357164
29. Huang, Y., Yang, L.-E., Luo, Q.-Z.: Free vibration of axially functionally graded Timoshenko beams with non-uniform cross-section. Compos. Part B Eng. **45**, 1493–1498 (2013). https://doi.org/10.1016/j.compositesb.2012.09.015
30. Abbas, B.A.H.: Dynamic stability of a rotating Timoshenko beam with a flexible root. J. Sound Vib. **108**, 25–32 (1986). https://doi.org/10.1016/S0022-460X(86)80308-X
31. Datta, P.K., Ganguli, R.: Vibration characteristics of a rotating blade with localized damage including the effects of shear deformation and rotary inertia. Comput. Struct. **36**, 1129–1133 (1990). https://doi.org/10.1016/0045-7949(90)90221-M
32. Ozgumus, O.O., Kaya, M.O.: Energy expressions and free vibration analysis of a rotating double tapered Timoshenko beam featuring bending-torsion coupling. Int. J. Eng. Sci. **45**, 562–586 (2007). https://doi.org/10.1016/j.ijengsci.2007.04.005
33. Ozgumus, O.O., Kaya, M.O.: Flapwise bending vibration analysis of a rotating double-tapered Timoshenko beam. Arch. Appl. Mech. **78**, 379–392 (2008). https://doi.org/10.1007/s00419-007-0158-5
34. Zhu, T.-L.: Free flapewise vibration analysis of rotating double-tapered Timoshenko beams. Arch. Appl. Mech. **82**, 479–494 (2012). https://doi.org/10.1007/s00419-011-0568-2
35. Lee, S.-Y., Lin, S.-M., Lin, Y.-S.: Instability and vibration of a rotating Timoshenko beam with precone. Int. J. Mech. Sci. **51**, 114–121 (2009). https://doi.org/10.1016/j.ijmecsci.2008.12.008
36. Rajasekaran, S.: Free vibration analysis of axially functionally graded tapered Timoshenko beams using differential transformation element method and differential quadrature element method of lowest-order. Appl. Math. Model. **37**, 4440–4463 (2013). https://doi.org/10.1007/s11012-013-9847-z
37. Chen, Y., Zhang, J., Zhang, H.: Free vibration analysis of rotating tapered Timoshenko beams via variational iteration method. J. Vib. Control **23**, 220–234 (2015). https://doi.org/10.1177/1077546315576431
38. Lee, H.P.: Buckling and dynamic stability of spinning pre-twisted beams under compressive axial loads. Int. J. Mech. Sci. **36**, 1011–1026 (1994). https://doi.org/10.1016/0020-7403(94)90024-8
39. Chen, C.K., Ho, S.H.: Transverse vibration of a rotating twisted Timoshenko beams under axial loading using differential transform. Int. J. Mech. Sci. **41**, 1339–1356 (1999). https://doi.org/10.1016/S0020-7403(98)00095-2
40. Yardimoglu, B., Yildirim, T.: Finite element model for vibration analysis of pre-twisted Timoshenko beam. J. Sound Vib. **273**, 741–754 (2004). https://doi.org/10.1016/j.jsv.2003.05.003
41. Lin, S.C., Hsiao, K.M.: Vibration analysis of a rotating Timoshenko beam. J. Sound Vib. **240**, 303–322 (2001). https://doi.org/10.1006/jsvi.2000.3234
42. Lee, S.Y., Sheu, J.J.: Free vibration of an extensible rotating inclined Timoshenko beam. J. Sound Vib. **304**, 606–624 (2007). https://doi.org/10.1016/j.jsv.2007.03.005
43. Ibrahim, S.M., Alsayed, S.H., Abbas, H., Carrera, E., Al-Salloum, Y.A., Almusallam, T.H.: Free vibration of tapered beams and plates based on unified beam theory. J. Vib. Control **20**, 2450–2463 (2014). https://doi.org/10.1177/1077546312473766
44. Ghafarian, M., Ariaei, A.: Free vibration analysis of a system of elastically interconnected rotating tapered Timoshenko beams using differential transform method. Int. J. Mech. Sci. **107**, 93–109 (2016). https://doi.org/10.1016/j.ijmecsci.2015.12.027
45. Yardimoglu, B.: A novel finite element model for vibration analysis of rotating tapered Timoshenko beam of equal strength. Finite Elem. Anal. Des. **46**, 838–842 (2010). https://doi.org/10.1016/j.finel.2010.05.003